IOP Concise Physics

Lattice Boltzmann Modeling of Complex Flows for Engineering Applications

Andrea Montessori and Giacomo Falcucci

Chapter 6

Lattice Boltzmann approach to reactive flows in nano-porous catalysts

The effective control and optimization of catalytic processes is known to have a crucial impact in many fields of applied science and technology, from the synthesis of new materials, to the production of innovative fuels and energy systems of crucial relevance to sustainable industrial growth [1, 2]. Due to the complex nature of the involved phenomena, it is characterized by timescales ranging from femtoseconds, $O(10^{-15}\text{s})$, bond breaking/forming events, all the way up to minutes and hours for reactor operation. Under such conditions, the experimental activity must be assisted by multiscale numerical models aimed at assessing the interplay of the different physical mechanisms involved in the process.

Multiscale computational models capable of describing reactive flows in monolithic catalytic media are urgently needed to assess the catalytic activity and stability of new catalyst materials such as the recently discovered class of monolithic nanoporous gold (np-Au) ([3, 4]). Despite the generally high stability of np-Au, reaction-induced coarsening of both pores and ligaments has recently been observed during oxidative coupling of alcohols under flow reactor conditions ([5]). The coarsening seems to depend strongly on the orientation of the sample with respect to the gas stream, with substantial coarsening of the rear surface, while the gas-facing side appears to be unaltered (see figure 6.1). This behaviour suggests substantially different local gas-surface chemistries on the up- and downstream catalyst surface. Here, multiscale computational models predicting the reactive flow through a monolithic catalytic sample can provide critical information about the local gas-surface chemistry and about the locations of reactions within the catalyst. Here, we report on the development of a predictive multiscale mass transport computational framework based on the LBM that allows further efficiency improvements by guiding the development of catalyst architectures.

doi:10.1088/978-1-6817-4672-2ch6

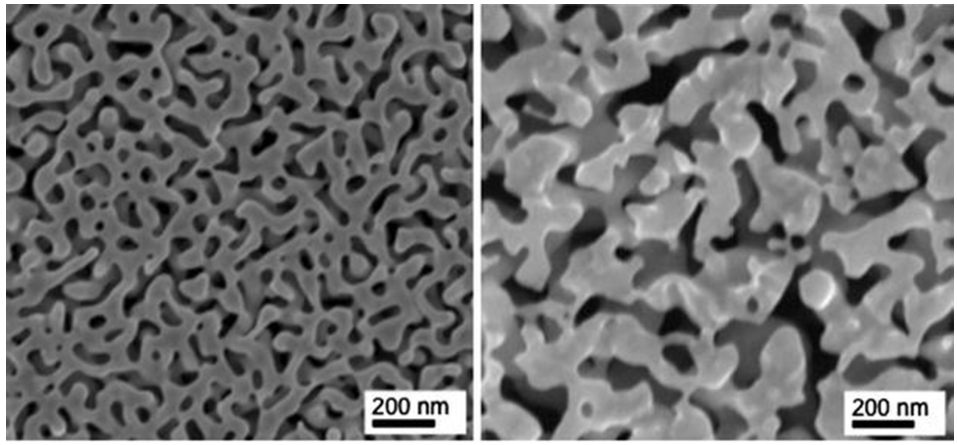

Figure 6.1. Evolution of the morphology of np-Au during oxidative coupling of alcohols in a flow reactor. SEM images of the surface of (a) bulk np-Au sample at the end of the experiment from a the surface facing the gas flow and (b) the surface opposite to the gas flow. The surface nanostructure is altered only on the surface facing the incoming gas stream [6].

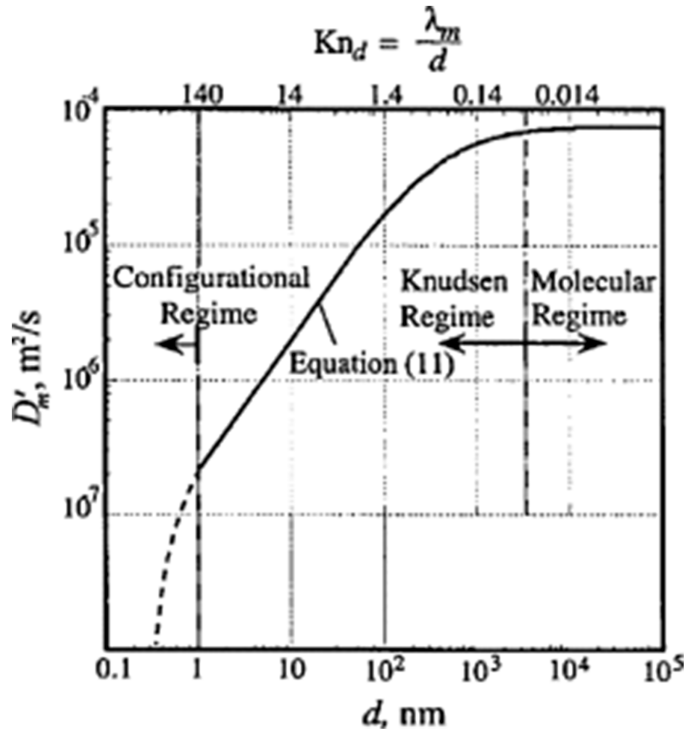

Figure 6.2. Dependence of the total diffusivity on pore diameter or, given a mean free molecular path, on *Kn*. In this figure 'Molecular Regime' denotes the low-Knudsen collective particle (hydrodynamic) regime, whereas 'Configurational Regime' stands for high-Knudsen free-particle motion. Note that Knudsen increases from right to left. From [8].

In this chapter, a recently developed model for mesoscale reactive flows in porous media that takes into consideration the nano- and microscale structure of the pores, is presented. From a macroscopic point of view, the physics of fluid–solid interactions is captured by appropriate boundary conditions, which specify the amount of mass, momentum and energy exchange between impinging and desorbing molecules.

When considering passively advected scalars in fluid flows, LBM allows one to tune the carrier kinematic viscosity independently from the passive scalar molecular diffusivities. Here, this unique characteristic to investigate flow reactivity in response to variations of molecular diffusivity within non-hydrodynamic regimes, is exploited.

In the following, the conversion efficiency predicted by our model is compared to the experimentally observed conversion rates for methanol oxidation over a nanoporous gold disc using a quartz tube microreactor. This catalyst has recently been reported to be highly effective for the selective oxidation of methanol to methyl formate ([3, 7]).

6.1 Relevant non-dimensional numbers in reactive flows

The main governing dimensionless parameters of reactive fluid transport are: the Reynolds number $Re = Ud/\nu$, measuring inertial versus dissipative effects, the Mach number $Ma = U/c_s$, fluid versus sound speed and the Knudsen $Kn = \nu/c_s d$, namely the molecular mean free path versus the average flow characteristic length scale. A second group is composed by the Peclét $Pe = Ud/D$ (advection over diffusion), advective Damkhler $Da_A = c_s p/U$ (chemical versus advection timescales), diffusive Damkhler $Da_D = c_s pd/D$, (chemical versus diffusive timescale) and Schmidt $Sc = \nu/D$ (momentum versus mass diffusion). The following notation is employed : U and d are respectively the characteristic pore velocity and spacing, ν is the fluid kinematic viscosity and D is the diffusivity of the chemical species.

It is possible to identify five quantities describing the physical system, namely, U, ν, D, d, c_s involving two physical dimensions, length and time. A straightforward application of the Π theorem allows one to formulate three independent non-dimensional groups.

Therefore, the following relations hold:

$$Kn = MaRe,\ Pe = ScRe,\ Da_D = PeDa_A$$

Given the three relations above, one is left with four independent parameters, Kn, Da_D, Pe, Sc. When the pore thickness is small compared to the mean-free path of the molecules, say $Kn > 1$, molecules collide with the pore surface with higher probability than bulk intermolecular collisions. The resulting total diffusivity, namely $1/Dtot = 1/D_M + 1/D_K$ gets lower where D_M and D_K are the molecular and Knudsen diffusion coefficients, respectively. The investigation of the dependence on the Kn is here restricted to $Pe = O(10^{-5})$, as it pertains to rarefied gas flows in catalytic media.

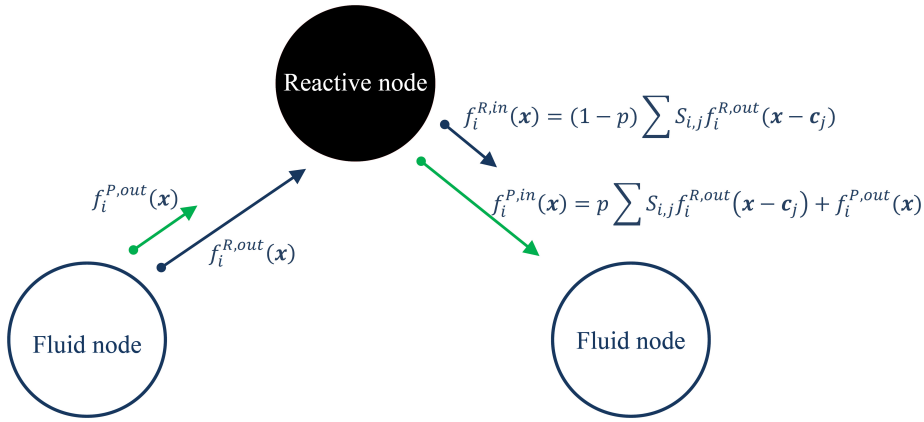

Figure 6.3. The sputtering reactive boundary condition.

6.2 The reactive boundary condition

Chemical reactions are patterned after the following methanol oxidation reaction [7],

$$2CH_3OH + O_2 \rightarrow HCOOCH_3 + 2H_2O, \tag{6.1}$$

Species interconversion due to catalytic reactions at the pore surface is accounted for by considering a local exchange of populations, as they meet and react on the solid walls of the pore. In the case of heterogeneous catalysis, such reaction takes place whenever gas populations hit the surface of the porous catalyst. Here, a first order chemical reaction of the generic form R → P is considered. The reactive boundary condition is designed such that, upon colliding with a solid site, the reactant R converts into the product P with a given probability p. Thus, each molecule of R colliding with a catalytic site is re-emitted along a random direction, either as species R with probability $1 - p$ (no-reaction), or as species P with probability p. It is worth highlighting that, in order to fulfill mass conservation locally, p is uniform in the domain and constant in time. Within this framework a typical chemical timescale can be defined as $\tau_{ch} = \Delta t/p = 1/p$ (in lattice units), which is the time interval needed for one representative molecule of product to enter the system (i.e. to be produced). First order surface chemical reactions have been modeled by implementing a sputtering boundary condition, as depicted in figure 6.4. In equations,

$$\begin{aligned} f_i^{\mathrm{R,in}}(\mathbf{x}) &= (1-p)\sum_{j=1}^{b(\mathbf{x})} S_{i,j} f_i^{\mathrm{R,out}}(\mathbf{x}-\mathbf{c}_j) \\ f_i^{\mathrm{P,in}}(\mathbf{x}) &= p\sum_{j=1}^{b(\mathbf{x})} S_{i,j} f_i^{\mathrm{R,out}}(\mathbf{x}-\mathbf{c}_j) \end{aligned} \tag{6.2}$$

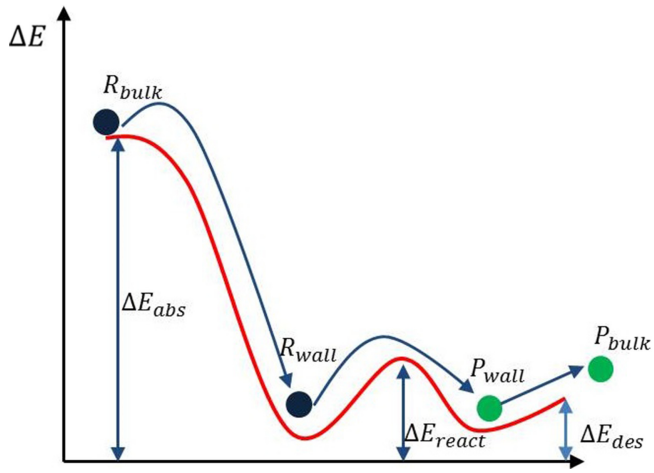

Figure 6.4. Sketch of the energetic landscape associated with absorption of reactants within the surface and desorption of reaction products back into the pore. Once they come sufficiently close to the surface, the reactants are attracted to it with an absorption energy of $\Delta E_{\text{abs}} \sim 0.8$–1 eV. Subsequently, they turn into products by going over an activation barrier of $\Delta E_{\text{react}} \sim 0.4$ eV. The reactant face with a much smaller desorption barrier of $\Delta E_{\text{des}} \sim 0.1$–0.2 eV

where $S_{i,j}$ is a random sputtering matrix obeying the mass conservation constraint, $\sum_{j=1}^{b(\mathbf{x})} S_{i,j} = 1$ and $0 \leqslant b(\mathbf{x}) \leqslant 8$ is the number of active links at any given lattice site $\mathbf{x}$. According to this model, each node of the porous medium in direct contact with the gas nodes acts as a catalytic site.

The boundary condition is built in such a way as to locally preserve the R + P mass, while the C mass is conserved anyway since the carrier does not take part in the reaction.

The random, although discrete, orientation of the emerging populations mimics the mesoscopic effect of the wall orientation on the gas dynamics and the fact that the particles that are adsorbed by the catalyst have sufficient time to randomize the desorption directions. In the present boundary condition (see figure 6.4) such randomization mechanism acts independently on all the chemical species, a choice motivated by the fact that, as the value of the Knudsen number increases, velocity slip becomes more and more apparent at the porous wall.

6.3 Consistency of reaction time

A key element of the present model in terms of comparison to experiment is the relative rate of reaction on the surface as compared to the diffusion rate throughout the nanoporous structure; the latter is captured by the values of *Re*, *Kn* and *Pe*. The former is taken into account by the value of *Da*, which depends on the chemical reaction time τ_{ch} . Here, an independent check of the chemical time scale value τ_{ch}, computed from the non-dimensional numbers in our simulations is provided, by comparing the numerical time scales and the time scale computed from *ab initio* density functional theory (DFT) calculations [9].

The characteristic time of the reaction τ_{ch} is a function of the time step expressed in physical units, Δt_{exp}, and the reaction probability p, $\tau_{ch} = \Delta t_{exp}/p$. Taking p as 0.45 and retrieving Δt_{exp} from the compliance between experimental and numerical viscosities ($\Delta t_{exp} = \nu_{LB}\Delta x^2/\nu_{exp}$), we have $\tau_{ch} \simeq 25$ ps. The reaction rate (inverse time scale) can be defined as $R = N_c A$, where N_c is the number of catalyst atoms in the lattice cell, A the Arrhenius factor $A = ke^{(-(E/(k_B T)))}$, with k the attempt rate (1/s). Given that the catalyst density is $n_c = 10$ atoms/(10 nm)^2, we estimate $Nc = 10$ atoms in a LBM cell; taking $k = 10^{13}\,\mathrm{s}^{-1}$, $E = 0.35$ eV and $T = 450$K (see [10]), which are typical values for the reactions considered here, we obtain an effective reaction rate:

$$R \simeq 1.0 \times 10^{10}\,\mathrm{s}^{-1}$$

As a result, the characteristic chemical time scale is equal to:

$$\tau_{ch} = 1/R \simeq 100\ \mathrm{ps}$$

that is, the same order of magnitude of τ_{ch} computed according to the simulation time step.

Considering the experimental value of the volumetric flow 50 mL/min corresponding to about $\dot{N} = 3 \times 10^{19}$ reactant molecules/s, and an effective reaction probability [11] $p_{eff} = 10^{-11}$ obtained from experimental measurements, we find $\dot{R} = \dot{N} p_{eff} \sim 3 \times 10^8$ reactions/s in the whole ingot.

We can further define the chemical time scale as $\tau_{ch} = (1/R)/(S/A)$, which is the ratio of the exposed surface area within the pores versus the area of the ingot gas-facing area. Based on digital reconstruction of the nanoporous material, we obtain $S/A \sim 200$ for a reactive ingot layer of about 10 μm in depth, which gives τ_{ch}, in close match with the values of the LBM evaluation and DFT prediction.

6.4 Numerical simulations

Numerical results of simulations on a numerical sample of nanoporous medium, with porosity of 70%, with random pore distribution, are here reported. Flow inside the medium has been obtained by applying a constant mass force to the carrier distribution, and imposing unit concentration along the inlet. Zero-gradient and periodic boundary conditions have been applied respectively on the outlet section and across all crossflow directions. Numerical simulations have been carried out by varying the Da_D and Kn numbers independently. The results are analyzed in terms of Depth of Penetration (DoP) of the reactant, which are defined as the distance from the inlet section at which 80% of the Reactant is consumed, that is where the average concentration on a crossflow section of the specimen, namely $\bar{C}$, falls below 20%. Reactant concentration hereinafter is normalized to the inlet reactant concentration.

6.5 Effect of the Damköhler number

In this subsection, the effect of the Damköhler number is studied. The Peclét number is chosen to be of order $O(10^{-4})$ in all the simulations in order to be consistent with the experimental flow conditions within the ingot nano-pores previously mentioned

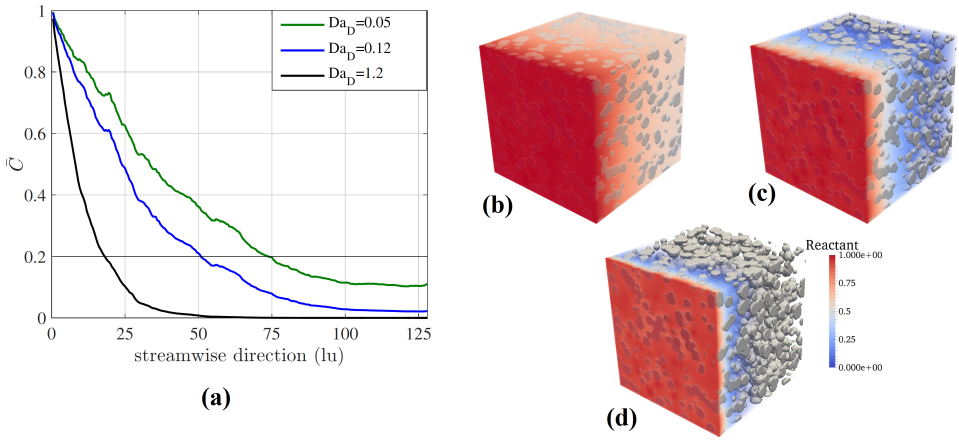

Figure 6.5. Reactant concentration across the sample for three different Da_D namely, (a) $Da_D = 0.05$, (b) $Da_D = 0.12$ and (c) $Da_D = 1.2$. The thick line at the 20% value identifies the assumed penetration threshold.

[6]. Indeed, by taking a typical flow discharge through the reactor of the order of 50 ml min^{-1} and an ingot diameter $\simeq$10 mm, the outside velocity can be estimated of the order 0.04 m s^{-1}. The effective diffusion coefficient inside the pores is estimated as $\simeq 10^{-6}$ m^2 s^{-1}. Given that the characteristic flow speeds inside the pore (roughly 50 nm in diameter) are lower (say by one or two orders of magnitude) than those outside, a Peclét number of $O(10^{-4})$ is an appropriate choice, giving a gas speed $\simeq 2 \cdot 10^{-3}$ m s^{-1} inside the pore. From figure 6.5(a), the major effect of Da on the depth of penetration is evident. The lower the Damköhler, the deeper the penetration of the reactant into the bulk of the nano-porous catalyst.

6.6 Effects of the Knudsen number

The procedure followed to carry out the simulations is here outlined: the scalar relaxation time defines the D_M, and consequently it is used to define the Da_D appearing in figure 6.7. The Knudsen number is varied acting on kinematic viscosity, through the relaxation rate, of the carrier. It is worth recalling here that at high Kn numbers, the total diffusivity (D_{tot}), receives a further contribution from D_K. The higher the D_{tot} the higher the reaction rate, since small pores, less affected by flux, become available to reaction [8].

With respect to figure 6.6, the higher the D_K the higher the D_{tot}, but D_{tot} reduces to D_M for $D_K \to \infty$. Since $D_K \propto d \propto \lambda/Kn$ then $D_K \propto 1/Kn$, therefore, the DoP automatically accounts for the effect of the total diffusivity, which is a decreasing function of the Kn. Here, the DoP at two different Kn (0.1 and 1) and three different Da_D (0.05, 0.12 and 1.2) is analyzed. In figure 6.7 the $\bar{C}$ profiles measure the coupled effect of the Kn and Da_D. The results show a strong decrease of the DoP at increasing Da_D. The results also show that the DoP is also a decreasing function of Kn. It is of interest to observe that the lower the D_M (that is higher Da_D), the lower the drop in

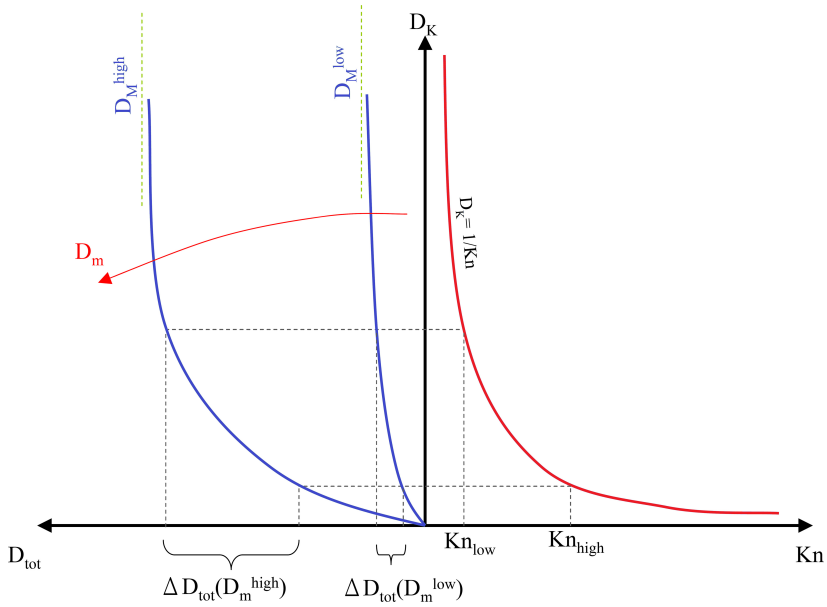

Figure 6.6. Qualitative sketch showing the dependency of the D_{tot} on the Kn through the D_K. The higher the Kn the higher the D_{tot}, but the effect is strongly mitigated by the value of D_M, that is, the higher the D_M the larger the gain in D_{tot}. Note that, for $Kn \to 0$, (hydrodynamic regime), $D_K \to \infty$ $D_{\text{tot}} \to D_M$.

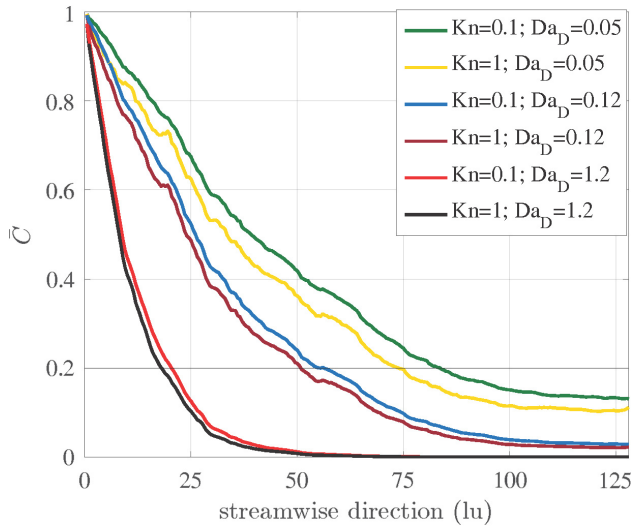

Figure 6.7. Combined effect of Da_D and Kn on the steady state distribution of $\bar{C}$ along the streamwise direction.

diffusivity caused by an order of magnitude of increase in Kn. This behavior is, at least qualitatively, in remarkable accordance to what is predicted by the theory and depicted in figure 6.6.

6.7 Upscaling

In [12] the numerical LBM solution is compared with the analytical solution of a steady 1D homogeneous reactive medium, fed by a constant rate of reactant, governed by the following equation:

$$U\frac{\partial C}{\partial x} = D\frac{\partial^2 C}{\partial x^2} + \frac{C}{\theta} \tag{6.3}$$

where $\theta = \Delta t/p$ is the characteristic chemical reactive time. Equation (6.3) can be cast in non-dimensional form:

$$Pe\frac{\partial C}{\partial x^*} = \frac{\partial^2 C}{\partial x^{*2}} + CDa_D \tag{6.4}$$

where $x^* = x/L$ is the dimensionless length. The solution of equation (6.4) is of the form $C(x^*) = \exp(-x^*/\delta)$, where $\delta = [1/2(Pe - \sqrt{4Da_D + Pe^2})]^{-1}$ is a characteristic non-dimensional length scale for the homogeneous reactive layer. In figure 6.8, the numerical solution is plotted together with the analytical aforementioned solution for the homogeneous medium calculated with Pe and Da_D pertaining to the simulation. It is clear that the idealised homogeneous medium is significantly more efficient, i.e. it yields a smaller reactive layer. In an upscaling perspective, one should determine δ as the best fit of the analytical solution to the numerical one. Such procedure, for the case considered, yields the concentration distribution shown in figure 6.8. The assessment of the effective reactive length δ represents a crucial step towards the multiscale simulation of catalytic devices of engineering relevance.

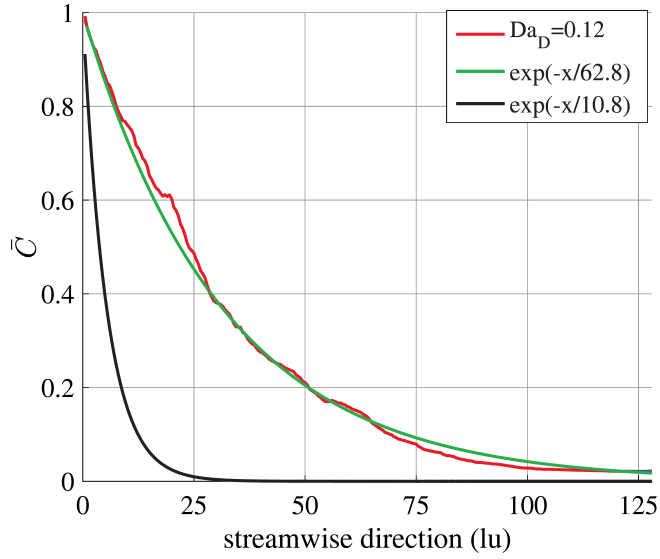

Figure 6.8. Best fit of the numerical solution gives delta = 62.8, i.e. about six times larger than the corresponding value for the homogeneous media. This reflects the reduced reactivity due to the porous structure of the material.

References

[1] Janardhanan V M and Deutschmann O 2006 CFD analysis of a solid oxide fuel cell with internal reforming: Coupled interactions of transport, heterogeneous catalysis and electrochemical processes *J. Power Sources* **162** 1192–202

[2] Park S, Gorte R J and Vohs J M 2000 Applications of heterogeneous catalysis in the direct oxidation of hydrocarbons in a solid-oxide fuel cell *Appl. Catal. A* **200** 55–61

[3] Wittstock A, Zielasek V, Biener J, Friend C M and Bäumer M 2010 Nanoporous gold catalysts for selective gas-phase oxidative coupling of methanol at low temperature *Science* **327** 319–22

[4] Wittstock A and Bäumer M 2013 Catalysis by unsupported skeletal gold catalysts *Acc. Chem. Res.* **47** 731–9

[5] Stowers K J, Madix R J, Biener M M, Biener J and Friend C M 2015 Facile ester synthesis on ag-modified nanoporous au: Oxidative coupling of ethanol and 1-butanol under uhv conditions *Catal. Lett.* **145** 1217–23

[6] Falcucci G *et al* 2016 Mapping reactive flow patterns in monolithic nanoporous catalysts *Microfluid. Nanofluid.* **20** 1–13

[7] Personick M L, Zugic B, Biener M M, Biener J, Madix R J and Friend C M 2015 Ozone-activated nanoporous gold: a stable and storable material for catalytic oxidation *ACS Catal.* **5** 4237–41

[8] Mezedur M M, Kaviany M and Moore W 2002 Effect of pore structure, randomness and size on effective mass diffusivity *AIChE J.* **48** 15–24

[9] Xu B, Haubrich J, Baker T A, Kaxiras E and Friend C M 2011 Theoretical study of o-assisted selective coupling of methanol on au (111) *J. Phys. Chem.* C **115** 3703–8

[10] di Staso G, Clercx H J H, Succi S and Toschi F 2016 DSMC-LBM mapping scheme for rarefied and non-rarefied gas flows *J. Comput. Sci.* **17** 357–69

[11] Wang L-C, Stowers K J, Zugic B, Personick M L, Biener M M, Biener J, Friend C M and Madix R J 2015 Exploiting basic principles to control the selectivity of the vapor phase catalytic oxidative cross-coupling of primary alcohols over nanoporous gold catalysts *J. Catal.* **329** 78–86

[12] Montessori A, Prestininzi P, la Rocca M, Falcucci G, Succi S and Kaxiras E 2016 Effects of knudsen diffusivity on the effective reactivity of nanoporous catalyst media *J. Comput. Sci.*